International Journal of Greenhouse Gas Control 134 (2024) 104128

Contents lists available at ScienceDirect

International Journal of Greenhouse Gas Control

journal homepage: www.elsevier.com/locate/ijggc

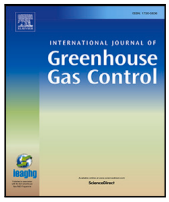

Impact of CO_2-rich seawater injection on the flow properties of basalts

Eleni Stavropoulou *, Cesare Griner, Lyesse Laloui

Ecole Polytechnique Fédérale de Lausanne (EPFL), Laboratory for Soil Mechanics (LMS), EPFL-ENAC-LMS, Station 18, CH-1015 Lausanne, Switzerland

ARTICLE INFO

Dataset link: https://zenodo.org/doi/10.5281/zenodo.10910995

Keywords:
Carbon mineralisation
Basalts
Pore network modelling
Flow properties
CO_2 storage

ABSTRACT

Permanent CO_2 storage in basalts through mineralisation offers a promising solution for reducing carbon emissions and mitigating climate change. This study focuses on the impact of potential mineralisation on the flow properties of the basaltic material. Fluid flow evolution before and after exposure to CO_2 dissolved in seawater is measured in terms of hydraulic conductivity and permeability under field-like conditions over 1 to 3.5 months. Permeability reduction of up to one order of magnitude suggests that porosity decreases due to mineral precipitation after CO_2 exposure. X-ray tomography measurements of the tested cores reveal a maximum porosity decrease of 1.5% at the given resolution (50 μm/px). To better understand eventual modifications of the connected pore network after mineralisation, fluid flow simulations are performed on the 3D pore network of the material that is reconstructed directly from the acquired x-ray images. A double porosity is proposed: macro-porosity as visible from the tomographies (pores > 50 μm) and micro-porosity (pores < 50 μm). To reproduce the post-CO_2 exposure flow, reduction of macro-porosity is not enough. Instead, a decrease of the micro-pores is necessary by up to 43%. The experimental and numerical results suggest that potential mineralisation can substantially modify the pore space of the intact basaltic material and consequently impact storage efficiency if flow is not preserved.

1. Introduction

Carbon Capture and Storage (CCS) is considered as one of the most effective technologies to mitigate increasing carbon emissions. CO_2 storage in basalts through mineralisation is a promising potentially cost-effective method that occurs rapidly, typically within 1–2 years (Matter et al., 2016; Clark et al., 2019), compared to CCS solutions in sedimentary reservoirs the timescale of which is significantly larger (Snæbjörnsdóttir et al., 2017). CO_2 is injected in the subsurface after being dissolved in water, at low over-pressures and shallow depth (a few hundreds of metres) in highly permeable locations. Injection of dissolved CO_2 enhances trapping safety as solubility has already taken place, while risk of leakage to the surface is limited since the injected fluid is not buoyant (Sigfusson et al., 2015). Finally, CO_2 injection at shallow depths results in reduced drilling and monitoring cost.

Storage potential in suitable basaltic formations is broad worldwide, both offshore and onshore (Snæbjörnsdóttir et al., 2020). In Europe, Carbfix has been exploring permanent CO_2 storage in basalts in Iceland with a total injected volume of nearly 100 kt CO_2 since 2014. Other large-scale projects include an ongoing project in Hawaii (De Paolo et al., 2021), or the Wallula project conducted in the USA, where supercritical CO_2 was injected into a basaltic formation, with estimates indicating up to 60% mineralisation within two years based on hydrological modelling (McGrail et al., 2017; White et al., 2020).

Even though storage of dissolved CO_2 in basalts offers potential advantages, a large implementation requires vast water amounts, making it ecologically inviable. The use of seawater as an alternative solvent is explored in Iceland, where seawater is readily available in proximity of the basaltic ocean crust, a reservoir with a storage potential of approximately $3 \cdot 10^5$ Gt CO_2 (Marieni et al., 2013). The efficiency of carbon mineralisation in seawater has been demonstrated using batch experiments with basalt and dissolved CO_2 in seawater (Voigt et al., 2021). A total mineralisation of up to 20% occurred within five months, corresponding to carbonation rates similar to those observed in basalt-freshwater-CO_2 experiments in both laboratory and field settings.

In December 2023, Carbfix launched the first field injection of CO_2 dissolved in seawater at the Helguvík site using Swiss-captured CO_2 (Becattini et al., 2022; Zappone et al., 2023). The injection targets a highly fractured location at a depth below 400 m. Existing studies show that potential porosity reduction (clogging) could significantly limit the material's storage capacity (Callow et al., 2018; Wu et al., 2021). Under constant injection rates, porosity reduction may lead to localised increase of pore pressure, decrease in effective stress, and triggering of seismic events. Due to the lack of seismic exploration campaigns in the injection area, information on the extension of the reservoir and its properties remains limited to date.

* Corresponding author.
E-mail address: eleni.stavropoulou@epfl.ch (E. Stavropoulou).

https://doi.org/10.1016/j.ijggc.2024.104128
Received 30 October 2023; Received in revised form 2 April 2024; Accepted 2 April 2024
Available online 18 April 2024

This study aims to provide a better understanding of potential CO_2 mineralisation and its impact on the fluid flow properties of the basaltic material through a series of experimental and numerical testing. For the first time, the evolution of the material's flow properties after exposure to dissolved CO_2 in seawater is studied on intact basaltic cores under field representative conditions. The potential impact of mineralisation on the material's pore structure is studied in 3D with X-ray computed tomography (XRCT). The X-ray tomographies are then used to build a 3D pore network of the core to simulate fluid flow and get new insights into the impact of mineralisation on the connected porosity of the rock. Moreover, the findings of this work are supported by the measurements of fluid pH and conductivity and by mineralogical analysis of the basaltic material.

2. Materials and methods

2.1. Sample characterisation

Basalts are finely grained igneous rocks with a mineral composition containing 45% to 85% mafic minerals. They are typically found in extrusive volcanic environments (Farooqui et al., 2009) and are considered to be well-suited for carbon mineralisation due to their significant content of divalent cations (Ca^{2+}, $Mg^{2}+$, Fe^{2+}) and the presence of highly reactive mineral compositions to dissolved CO_2 such as pyroxene and olivine (Snæbjörnsdóttir et al., 2020).

Seven basaltic cores (diameter = 49 mm) from three different boreholes (HB-05, HB-0769 and HB-08) of shallow depth in the Holmsberg cliff near Helguvik, where a distinctive lava flow bedding was identified, are used in this study. Because basalt is formed from the rapid cooling of lava, the cores present an extremely heterogeneous porous structure that is obvious with naked eye. The different cores are selected aiming at targeting different field locations of variable pore structure and they have been cut down to cylindrical samples with a height over diameter ratio equal to 2. More precisely, samples 05–03, 07-01, 07-02, 08-02 and 08-03 are sized down to a diameter d = 38 mm and height h = 76 mm, while for samples 05-01 and 05-02 the original core diameter is preserved (d = 49 mm) with a height h = 98 mm.

The 3D porosity of each core is measured from XRCT images with an average pixel size equal to 50 μm and it is plotted with the corresponding depth of origin in Fig. 1. The calculated porosity values of the cores range between ≈ 3% and 20%, and unlike sedimentary rocks, there is no clear correlation between porosity and depth. Additional porosity results are included in the same figure, that have been acquired in the lab using the resaturation method (calculation of water volume based on mass decrease after drying in 80 °C). The two porosity measurements are comparable for all samples, except for sample 08-03 where a larger discrepancy between the porosity values is measured. This is due to the pre-existing large cavity (see 08-03 photo in Fig. 1) that was filled in with filled with a high-strength resin (HIT-HY 170 injection mortar) and was not considered in the XRCT analysis.

Structural heterogeneity is not encountered only between the different cores, but also within a core itself. Fig. 2 shows three horizontal slices of the XRCT scan of core 08-03 at different heights (A, B and C) as well as the corresponding segmented pores. The calculated 2D porosity at each height level varies significantly from bottom to top with values ranging from 1.98% to 9.45%. Moreover, the horizontal slices of the XRCT image reveal that micro-structural heterogeneity does not only manifest in terms of porosity level but also in terms of pore distribution (e.g. by comparing slices A and B that have similar total porosity but different pore topology). Considering carbon mineralisation, this is of particular importance when studying the flow properties of a material as they are directly related to the connectivity of the pore network.

Measurement of the pore size range has been performed using the Mercury Intrusion Porosimetry (MIP) method. The pore size distribution (PSD) of the basaltic material presents three distinct peaks with diameter values ranging from 0.01 μm to 100 μm (Fig. 3). This result reveals an additional group of micro-pores that cannot be detected by the XRCT images. The dominant pore size diameter of these micro-pores is measured in the range between 0.5 μm and 1.4 μm.

Table 1
Mineralogical composition of three basaltic samples.

sample	andesine (%)	augite (%)	olivine (%)
05-02	61	32	5
08-02	54	26	19
08-03	61	25	13

Table 2
Composition of synthetic seawater per 1000 g of demineralised water.

NaCl	$MgCl_2$	$MgSO_4$	$CaCl_2$	KCl	$NaHCO_3$
26.52 g	2.44 g	3.30 g	1.14 g	0.72 g	0.20 g

The mineralogical content of three samples (05-02, 08-02 and 08-03) has been measured with X-ray diffraction (XRD). As shown in Table 1, it principally consists of plagioclase (andesine), pyroxene (augite) and olivine. An additional small percentage of 2% of iron oxide (Fe_2O_3) has been detected in sample 05-02. Note that amorphous glass cannot be detected by XRD.

2.2. Experimental setup

The flow properties of the cores before and after exposure to CO_2-rich seawater are measured in the lab using the experimental setup presented in Fig. 4. First, the sample is confined under 5 MPa pressure with the aid of a sealing membrane. Resaturation is then performed using synthetic water, the composition of which is presented in Table 2 and is similar to that used by Voigt et al. (2021). To ensure homogeneous resaturation and distribution of pore pressure at the top and bottom, a porous disc is placed on either side of the sample. The flow properties are then measured in terms of hydraulic conductivity and permeability by applying a constant hydraulic gradient along the longest axis of the core (Darcy, 1856; Renard et al., 2001). More precisely, a ΔP = 1 MPa pore pressure gradient is applied between the upstream (2 MPa) and downstream (1 MPa) sides of the sample as illustrated in Fig. 4. Based on the Darcy's law, the absolute permeability k (m^2) of the core is calculated according to Eq. (1), by considering the corresponding hydraulic conductivity K (m/s), the fluid density (ρ_f = 1.02 g/cm^3), the acceleration of gravity g (m/s^2) and the fluid's dynamic viscosity($\eta_f = 1.05 \cdot 10^{-3}$ Pa s) at the temperature of the tests (21 °C) (Sharqawy et al., 2010):

$$k = K \frac{\eta_f}{\rho_f \cdot g} \tag{1}$$

The hydraulic conductivity of the core is calculated according to Eq. (2):

$$K = Q_f \frac{\rho_f \cdot g \cdot L}{A \cdot \Delta P_f} \tag{2}$$

where Q_f (m^3/s) is the volumetric flow, L (m) is the height of the sample, A (m^2) is the area section of the sample, and ΔP_f (Pa) is the applied pressure difference.

After assessing the initial flow properties of the material, CO_2-rich seawater is injected. CO_2 dissolution in seawater takes place in a reservoir at 2 MPa pressure and 20% volume concentration (see Fig. 4-b). More precisely, 80% of the reservoir volume is filled up with seawater and the remaining 20% is filled up with CO_2 introduced with a syringe pump at 2 MPa until volume stabilisation (zero CO_2 flow). The applied CO_2 concentration is ≈ 5 times higher than that applied in the field by Carbfix (Snæbjörnsdóttir et al., 2020) in order to accelerate the mineralisation process due to lower pH (Gysi and Stefánsson, 2012) and test multiple rock samples over a limited time, that ranges between

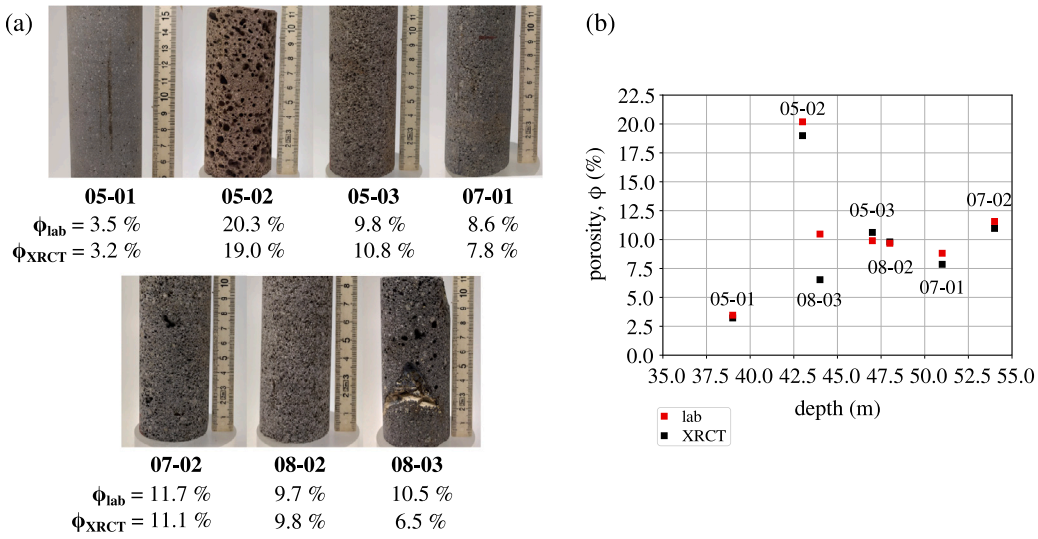

Fig. 1. Basaltic cores: (a) photographs of the seven basaltic cores; (b) core porosity (measured in the lab and from XRCT) as a function of core depth.

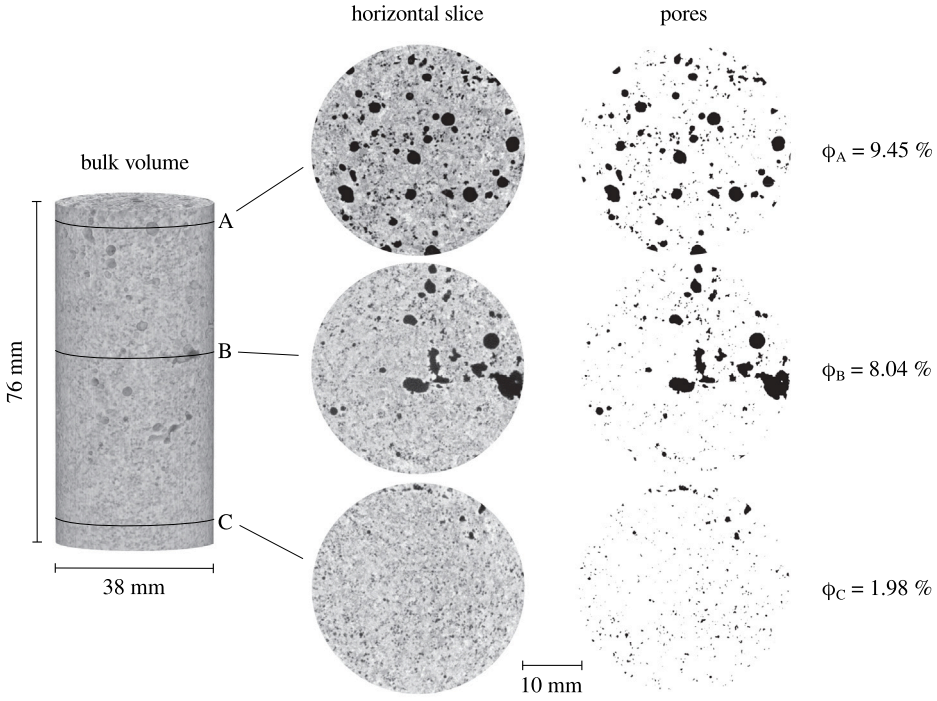

Fig. 2. XRCT volume of core 08-03 and horizontal slices at three height levels, in which 2D porosity is calculated (average porosity per slice).

1 and 3.5 months. The average exposure time is relevant to the time-scale of the results by Voigt et al. (2021), where pH and mineral composition changes of seawater are observed after 50 days interaction with basalt and CO_2. Based on the XRCT calculated pore volume, dissolved CO_2 twice the pore volume of the sample is injected. The sample is then exposed to CO_2-rich seawater under no-flow conditions at 5 MPa confining pressure (P_c) and 1.5 MPa pore pressure (P_p), i.e. 3.5 MPa differential pressure ($P_{diff} = P_c - P_p$). Finally, the hydraulic conductivity of the sample is measured after exposure to dissolved CO_2 by applying the same constant head method (ΔP = 1 MPa) to evaluate eventual flow changes related to carbon mineralisation. The experimental stages described above are summarised in Fig. 5 and have been applied without in between unmounting of the sample at 21 °C. Note that the temperature at the injection subsurface ranges between 30 °C and 50 °C (Matter et al., 2009).

2.3. Pore network model

To understand how mineralisation may affect the pore structure of the basaltic material, all cores have been scanned with XRCT (pixel size 50 μm) before and after exposure to dissolved CO_2. As shown in Fig. 2, the pore space of the core 08-03 exhibits significant heterogeneity, with larger pores located at the upper regions and denser zones towards the bottom of the given sample. Despite the presence of relatively large pores (some even reaching up to 1 cm), fluid flow is predominantly attributed to the connected porosity of the material. It is thus of major importance to characterise the connectivity of the tested sample.

To reproduce the experimental flow results, fluid flow simulations were performed using the open-source software OpenPNM (Gostick et al., 2016). The 3D pore network of the material was extracted from the acquired XRCT images using the SNOW algorithm (Gostick, 2017),

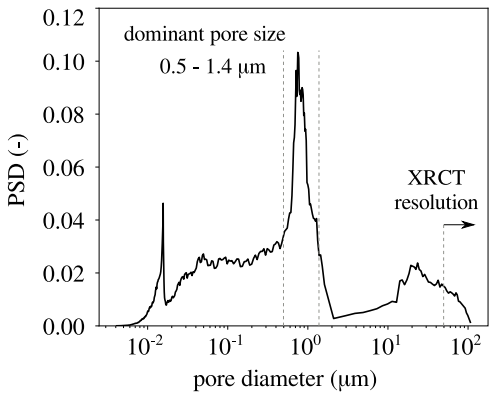

Fig. 3. Pore size distribution of basalt from the MIP method.

which defines the pore regions based on a watershed segmentation method that calculates a distance map from the solid matrix. The pore space is then described as a network of pores connected by throats, that in this study, are represented by spheres and cylinders respectively. To overcome resolution limitations from the input XRCT images, a double-scale porosity is considered: *macro*-porosity, corresponding to the pores visible in XRCT (> 50 μm), and *micro*-porosity, representing all pores below the pixel size of the XRCT images (< 50 μm). Introduction of micro-porosity enables the generation of a fully connected network where flow can be simulated throughout the entire core (see details in Section 3.2). Fluid flow simulations are performed by considering the Hagen–Poiseuille equation:

$$Q_{i,j} = \Delta P_{i,j} \frac{\pi \cdot r_{i,j}^4}{8 \cdot \mu_f \cdot L_{i,j}} \quad (3)$$

where $Q_{i,j}$ (m^3/s) is the volumetric flow rate between the pores i and j, $\Delta P_{i,j}$ (Pa) is the pressure difference between two consecutive pores i and j, $r_{i,j}$ (m) is the radius of the throat connecting the two pores i and j, μ_f (Pa s) is the dynamic viscosity of the fluid, and $L_{i,j}$ (m) is the distance between the two pores i and j.

In the model, the net flow rate is obtained by summing up the flow rate of all pores, and the absolute permeability of the network is calculated using the Darcy law (see Eq. (1)). In this work, single-phase laminar flow simulations are considered.

3. Results

3.1. Variation in flow properties

The experimental flow results, the exposure time and the corresponding porosity measurements from XRCT before and after CO_2 exposure are listed in Table 3. The initially measured hydraulic conductivity and permeability of the different samples are within a range from $\approx 10^{-10}$ to 10^{-7} m/s and $\approx 10^{-17}$ to 10^{-14} m^2, respectively. The obtained range of permeability is comparable to the experimental results reported by Callow et al. (2018) during flow tests in a core from Hellisheidi in Iceland, with mineral water under a differential pressure of 4 MPa ($k \approx 10^{-15}$ m^2). The higher permeability in this earlier study can be explained by a higher porosity of their sample (26.2%), as well as by the lower height/diameter ratio of the tested sample (0.6 instead of 2.0 in the current study).

Earlier data on the absolute permeability (k) of vesicular basalts and young oceanic crust range between 10^{-9} and 10^{-14} m^2 (Fisher, 1998; Saar and Manga, 1999). Field-scale reservoir modelling of the Carbfix site reported horizontal and vertical absolute permeabilities (k_h and k_v) between $3.0 \cdot 10^{-13}$ m^2 and $1.7 \cdot 10^{-12}$ m^2, respectively (Aradóttir et al., 2012). In the work by Callow et al. (2018), simulations of absolute permeability based on XRCT-acquired geometry calculated horizontal (k_h) and vertical absolute permeabilities (k_v) of $5.10 \cdot 10^{-11}$ m^2 and $2.07 \cdot 10^{-10}$ m^2, respectively.

The initial hydraulic conductivity is plotted with the corresponding porosity in Fig. 6 (square points). A proportional trend can be observed at low flow levels (10^{-8} m/s), whereas for higher flow levels, a larger variability in the correlation with porosity is denoted. The hydraulic conductivity and the corresponding porosity after CO_2 exposure (triangular points) show no trend between the different basaltic samples. To evaluate the changes of hydraulic conductivity before and after CO_2 exposure the ratio between the initial (K_i) and final (K_f) values is calculated in Table 3. Note that K_i/K_f is equal to the permeability ratio k_i/k_f. Changes in flow are negligible in four cores (05-01, 05-03, 07-01, and 07-02) where $K_i/K_f \approx 1$. For samples 05-02, 08-02 and 08-03, decrease of hydraulic conductivity by up to one order of magnitude is observed. These samples, noted with (*) in Table 3, will be considered for further pore network analysis. Flow decrease is supported by the decrease of the measured porosity in samples 08-02 and 08-03. However, no porosity changes were captured for sample 05-02, i.e. the sample with the highest porosity.

The four samples without significant variation in hydraulic conductivity (samples 05-01, 05-03, 07-01, and 07-02) present both increasing ($K_i/K_f < 1$) and decreasing ($K_i/K_f > 1$) flow and porosity properties after CO_2 exposure. Flow increase due to dissolution of basalt minerals and glass can occur during injection of acidic fluid (Snæbjörnsdóttir et al., 2018). Under these conditions carbonate precipitation can occur upon availability of divalent cations (e.g. Ca^{2+}, Ma^{2+}, Fe^{2+} in basalts). The mineralogical composition of the tested samples shows variation that can induce a different geochemical response.

3.2. Flow simulations

The measured reduction in hydraulic conductivity is in line with the calculated porosity evolution from the XRCT images for samples 08-02 and 08-03. In sample 08-02, the initial porosity of 9.8% decreases to 8.3% after 110 days exposure to dissolved CO_2. In sample 08-03, porosity diminishes from 6.5% to 5.2% after 60 days. It is important however to point out that at the given resolution (pore space lower than 50 μm is not detected), identifying precise regions of modified pore architecture is not obvious. In sample 05-02, even though hydraulic conductivity decreased by half an order of magnitude after 28 days of CO_2 exposure, no porosity changes were detected by XRCT. To gain a better insight into localised changes of the pore network of the material due to potential mineral precipitation, fluid flow simulations have been performed in these three samples.

The 3D pore network of each sample is calculated using the acquired XRCT images before and after exposure to CO_2. At the given image resolution, the pore structure is poorly connected making flow throughout the entire height of the sample impossible. In other words, the visible pores (> 50 μm) are located too far from their nearest pores to be assigned with connecting throat according to the watershed algorithm as detailed in Gostick (2017). Zahasky et al. (2018) performed a similar flow analysis on a basaltic sample (from Hellisheidi in Iceland), using XRCT with similar voxel resolution. To define the connected porosity, an additional clinical positron emission tomography (PET) analysis was performed to image flow pathways. In our study, a hypothesis of a fully connected network is made with the introduction of a micro-porosity that represents the solid matrix porosity of the material that, even though existent as shown from the MIP analysis (Fig. 3), it is not detectable from the XRCT. Based on the proposed approach, the not connected pores are manually connected to the rest of the network, based on the methodology explained in Appendix A. Fig. 7 shows the different steps to generate a fully connected pore network from 3D XRCT images. Single-phase flow simulation is then performed under conditions (pore pressure and fluid properties) similar to the hydromechanical tests in the lab.

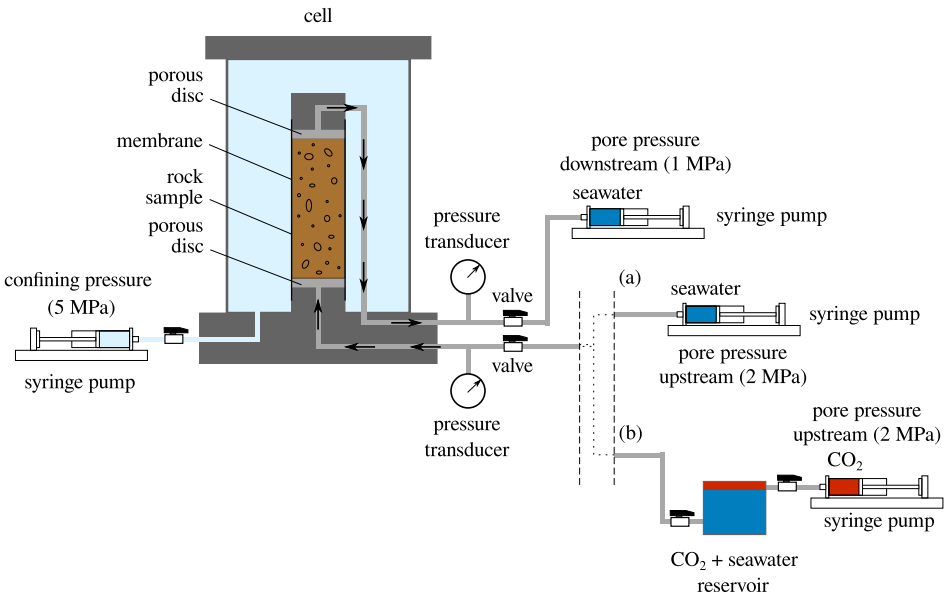

Fig. 4. Experimental setup for flow characterisation: (a) CO_2-rich seawater injection and (b) long-term CO_2-rich seawater exposure.

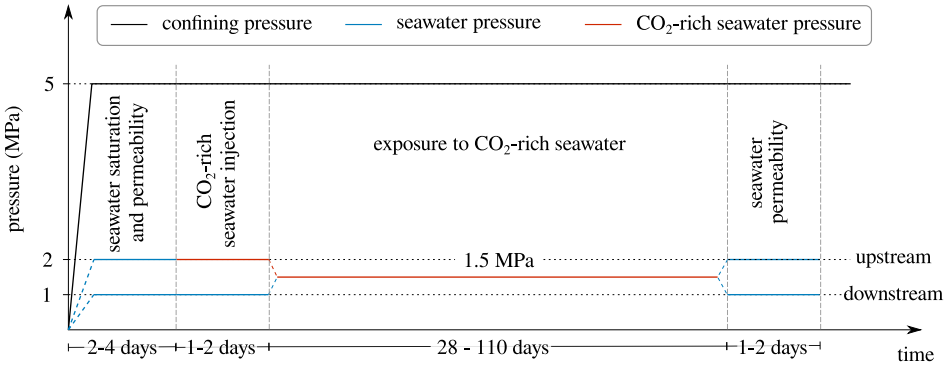

Fig. 5. Experimental timeline: application of confinement (5 MPa), saturation of the sample with seawater, assessment of permeability (ΔP = 1 MPa), injection of CO_2-rich seawater, long-term exposure of CO_2-rich seawater (1.5 MPa), post-exposure permeability (ΔP = 1 MPa).

Table 3
Hydraulic conductivity, permeability and porosity measured before and after exposure to CO_2. Samples noted with asterisk (*) are those with higher reduction in flow.

sample	CO_2 exposure	before CO_2 exposure			after CO_2 exposure			K_i / K_f
		K_i (m/s)	k_i (m^2)	ϕ_i (%)	K_f (m/s)	k_f (m^2)	ϕ_i (%)	k_i / k_f
05-01	33 days	$8.35 \cdot 10^{-10}$	$8.64 \cdot 10^{-17}$	3.2	$8.55 \cdot 10^{-10}$	$8.85 \cdot 10^{-17}$	3.9	0.97
05-02*	28 days	$1.06 \cdot 10^{-7}$	$1.09 \cdot 10^{-14}$	19.0	$7.35 \cdot 10^{-8}$	$7.60 \cdot 10^{-15}$	19.0	1.43
05-03	31 days	$6.02 \cdot 10^{-8}$	$6.23 \cdot 10^{-15}$	10.8	$5.59 \cdot 10^{-8}$	$5.78 \cdot 10^{-15}$	10.4	1.08
07-01	28 days	$1.51 \cdot 10^{-8}$	$1.56 \cdot 10^{-15}$	7.8	$1.65 \cdot 10^{-8}$	$1.70 \cdot 10^{-15}$	10.3	0.92
07-02	85 days	$1.58 \cdot 10^{-8}$	$1.64 \cdot 10^{-15}$	9.8	$1.79 \cdot 10^{-8}$	$1.85 \cdot 10^{-15}$	11.0	0.88
08-02*	110 days	$1.83 \cdot 10^{-7}$	$1.90 \cdot 10^{-14}$	9.8	$1.81 \cdot 10^{-8}$	$1.88 \cdot 10^{-15}$	8.3	10.1
08-03*	60 days	$1.65 \cdot 10^{-9}$	$1.71 \cdot 10^{-16}$	6.5	$7.32 \cdot 10^{-10}$	$7.57 \cdot 10^{-17}$	5.2	2.26

Table 4
Comparison of experimental and numerical results considering a single pore diameter and a pore size distribution that represent the micro-porosity of the solid matrix.

sample	K_{exp}(m/s)	k_{exp}(m^2)	solid matrix: single pore size			solid matrix: pore size distribution		
			d (μm)	$K_{num,\ d}$(m/s)	$k_{num,\ d}$(m^2)	mean_d (μm)	$K_{num,\ PSD}$(m/s)	$k_{num,\ PSD}$(m^2)
05-02								
pre CO_2	$1.06\cdot10^{-7}$	$1.09\cdot10^{-14}$	5.39	$1.06\cdot10^{-7}$	$1.12\cdot10^{-14}$	5.42	$1.06\cdot10^{-7}$	$1.10\cdot10^{-14}$
post CO_2	$7.35\cdot10^{-8}$	$7.60\cdot10^{-15}$	4.02	$7.37\cdot10^{-8}$	$7.78\cdot10^{-15}$	4.06	$7.50\cdot10^{-8}$	$7.91\cdot10^{-15}$
08-02								
pre CO_2	$1.83\cdot10^{-7}$	$1.90\cdot10^{-14}$	6.58	$1.82\cdot10^{-7}$	$1.92\cdot10^{-14}$	6.63	$1.83\cdot10^{-7}$	$1.93\cdot10^{-14}$
post CO_2	$1.81\cdot10^{-8}$	$1.88\cdot10^{-15}$	2.92	$1.80\cdot10^{-8}$	$1.90\cdot10^{-15}$	2.92	$1.85\cdot10^{-8}$	$1.95\cdot10^{-15}$
08-03								
pre CO_2	$1.65\cdot10^{-9}$	$1.71\cdot10^{-16}$	2.83	$1.65\cdot10^{-9}$	$1.75\cdot10^{-16}$	2.86	$1.65\cdot10^{-9}$	$1.74\cdot10^{-16}$
post CO_2	$7.32\cdot10^{-10}$	$7.57\cdot10^{-17}$	2.53	$7.34\cdot10^{-10}$	$7.74\cdot10^{-17}$	2.48	$7.32\cdot10^{-10}$	$7.72\cdot10^{-17}$

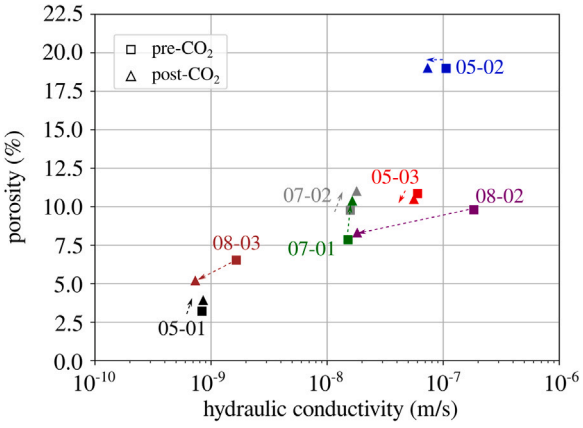

Fig. 6. Porosity and hydraulic conductivity before and after CO_2 exposure.

To represent solid matrix micro-porosity, a size diameter smaller than the minimum throat diameter of the initially generated pore network is assigned to the manually added throats. The connectivity of the material is thus represented by a double-scale porosity: macro-porosity (pores > 50 μm) and micro-porosity (solid matrix < 50 μm). Note that micro-porosity does not refer to additional pores but to the added throats to represent solid matrix and corresponds to 3.6%, 5.0% and 3.7% of the total porosity in samples 05-02, 08-02 and 08-03 respectively. Two approaches are considered for ascribing the throat size of solid matrix micro-porosity: a single diameter size and a pore size distribution.

First, a simpler case where a single throat diameter is assigned in the added throats is studied. The best fitted diameter is calculated (micrometric scale) with an iterative process to achieve the minimum difference employing the experimentally measured hydraulic conductivity. The calculated solid matrix diameter of the pre-CO_2 exposure network varies from 2.83 to 6.58 μm (i.e. 10 times lower than the XRCT resolution). To reproduce the post-CO_2 exposure results, a lower solid matrix diameter is calculated, ranging from 2.53 to 4.02 μm. The calculated solid matrix diameter (d) and the resulting hydraulic conductivity (K_{num}) and permeability (k_{num}), before and after CO_2 exposure, are presented in Table 4 for the three samples analysed. In the samples, a reduced solid matrix diameter is calculated from the post-exposure image, revealing a reduced micro-porous volume.

For a more realistic simulation of the solid matrix micro-porosity of the material, a lognormal PSD was assigned to the manually added throats. The mean (μ_d) with a fixed standard deviation ($\sigma_d = 0.15$) was calculated to best reproduce the experimentally measured hydraulic conductivity. The mean diameter of the added micro-porosity is equal to mean_d $= \exp(\mu_d + \frac{\sigma_d^2}{2})$ and the calculated value for each core is presented in Table 4. As expected, the best fitted mean diameter is similar to the single-diameter approach, with values ranging between 2.86 μm and 6.63 μm for the pre-CO_2 state, and from 2.48 μm and 4.06 μm for the post-CO_2 state. A reduced mean solid matrix diameter, and thus a reduced micro-porosity, is calculated from the post-exposure image. To reduce the calculation error introduced by the PSD's standard deviation, the reported hydraulic conductivity and permeability values correspond to the average result from ten simulations.

To evaluate the impact of porosity reduction as measured from XRCT on the flow response of the sample, the diameter of the macro-pores (> 50 μm) of the initial pore network (before CO_2 injection) are reduced by the measured amount for samples 08-02 and 08-03, as shown in Table 5. Flow simulation of the modified macro-porosity network results in no reduction of hydraulic conductivity (from 1.83 $\cdot10^{-7}$ m/s to 1.81 $\cdot10^{-7}$ m/s for sample 08-02 and from 1.65 $\cdot10^{-7}$ m/s to 1.64 $\cdot10^{-7}$ m/s for sample 08-03). This response suggests that mineralisation in the macro-pores does not have any significant impact on the flow properties of the material. Instead, additional reduction of the solid matrix porosity (micro-porosity < 50 μm) is necessary to reproduce the reduced post-exposure flow response.

The solid matrix diameter reduction for each sample is presented in Table 5 for both single-diameter and PSD approaches. A micro-porosity reduction up to ≈ 43% is calculated in sample 08-02 with both approaches (single-diameter and PSD) after 110 days of CO_2 exposure. A reduced micro-porosity by ≈ 18% is calculated (for both single-diameter and PSD) for sample 08-03 after 60 days of exposure. After 28 days exposure, micro-porosity reduction by 8.7% and 5.4% is calculated for sample 05-02 with each approach (single and PSD, respectively). These results reveal that carbon mineralisation is more prone to occur in the micro-pores, leading to a reduced flow response of the material by half to one order of magnitude.

Micro-porosity reduction can be crucial for storage efficiency since pore clogging can result in interruption of flow and consequently of mineralisation. The pore pressure propagation calculated throughout each sample before and after CO_2 exposure is plotted in Fig. 8. A different pressure front before and after CO_2 exposure is obtained. In sample 08-02, the creation of localised fingers is noted in the post-exposure pore pressure distribution. This localised response is driven by the occurred mineralisation that alters the initial pore space of the material. The pore-pressure front of sample 08-03 after CO_2 exposure reveals a localised zone of increased pressure gradient that

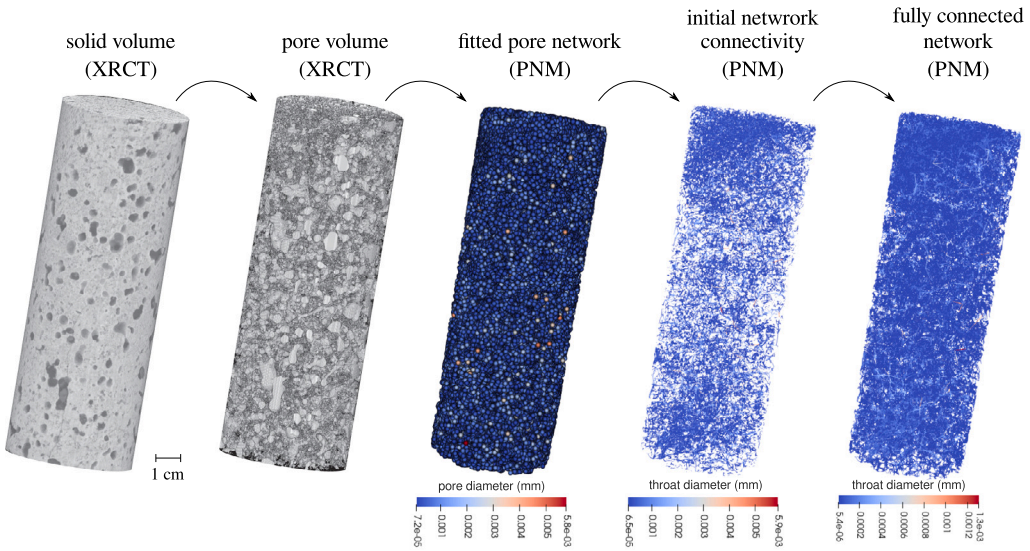

Fig. 7. Different steps for the creation of a fully connected pore network from an X-ray tomography of the studied rock sample (05-02). Note that in the XRCT solid volume, pores are in dark and solid in bright, whereas in the XRCT pore volume, pores are in bright and solid in dark.

Table 5
Porosity reduction of the pre-CO_2 network for reproducing the post-CO_2 flow results.

sample	CO_2 exposure	macro-pores reduction (XRCT)	micro-pores reduction (PNM)	
			single-diameter	PSD
05-02	28 days	0.0 %	5.39 μm → 4.92 μm: 8.7 %	5.42 μm → 4.95 μm: 5.4 %
08-02	110 days	1.5 %	6.58 μm → 3.70 μm: 43.7 %	6.63 μm → 3.75 μm: 43.4 %
08-03	60 days	1.3 %	2.83 μm → 2.31 μm: 18.4 %	2.86 μm → 2.34 μm: 18.2 %

suggests local pore clogging. This localised phenomenon is driven by the micro-structural heterogeneity of the material that has to be taken into account for appropriately characterising the efficiency and safety of CO_2 storage. Finally, in sample 05-02, a pre-existing micro-fissure serves as a preferential flow path which disappears in the post-exposure network. This pre-existing fissure is apparent in both XRCT images before and after exposure. Its volume evolution, however, is difficult to accurately quantify as it falls in the limit of the image resolution (see Appendix B). The obtained modified pore pressure propagation suggests that micro-fissures favour mineralisation as mentioned by Wu et al. (2021).

It is important to highlight that the resulting pore pressure propagation front is not affected by a variable pore size distribution of the assigned micro-porosity. The overall and localised fronts are reproducible (see Appendix C), even though no striking evolution of total macro-porosity can been detected by XRCT at the given resolution. The obtained evolution of the post-CO_2 network, therefore, suggests localised structural modifications during CO_2 exposure.

4. CO_2 mineralisation

Dissolution of CO_2 in water results in water acidification (Matter et al., 2009). Acidified water reacts with basalt and dissolves the primary minerals of the rock (Goldberg et al., 2008). Dissolution reactions release divalent cations into the solution (Ca^{2+}, Mg^{2+}, Fe^{2+}) that react with dissolved CO_2 and may precipitate to form stable carbonate minerals such as calcite ($CaCO_3$), magnesite ($MgCO_3$), and siderite ($FeCO_3$) (Khatiwada et al., 2012; Gislason et al., 2014). Both dissolution and precipitation processes are influenced by several factors, namely the relative amount and thermodynamic stability of primary minerals in the basalt, the composition of the injected fluid and the mineral dissolution/precipitation rates. For example, altered basalts containing serpentine instead of olivine may exhibit a lower rate of carbonation when compared to unaltered basalts that are rich in olivine (9% olivine content) (Liu et al., 2019). Moreover, secondary minerals such as clays and zeolites have the potential to form and compete with other reactions for the leached cations (Aradóttir et al., 2011).

As stated by Snæbjörnsdóttir et al. (2018), more than 90% of the crystalline fraction of the CarbFix subsurface storage consists of plagioclase, pyroxene and olivine and to a lesser extent of iron oxides and glass. Samples 08-02 and 08-03 have a higher content in olivine than sample 05-02, that in combination with a longer exposure time (60 and 110 days compared to 28 days, respectively) can favour increased carbon mineralisation.

Pore fluid of sample 08-02 has been measured to investigate whether carbon mineralisation occurred during the given exposure period (110 days). The electrolytic conductivity (mS/cm) of the used seawater, before and after being flushed through the basaltic core, as well as that of the CO_2-rich seawater after the end of the exposure period was measured. The measured conductivity of the initial solution (47.65 mS/cm) is slightly higher than that flushed through the rock sample (44.99 mS/cm). This slight decrease in conductivity (less than 3.00 mS/cm) suggests formation of some phases in the core. The conductivity of the post-CO_2 seawater is considerably lower (28.30 mS/cm) indicating a decrease in the concentration of cations due to precipitation of carbonates (mineralisation).

Moreover, the increase in pH from an acidic value (seawater + CO_2) to 6.57 (seawater + basalt) and 7.18 (seawater + CO_2) indicated a probable precipitation of carbonates. These fluid analysis results combined with the measured permeability reduction support potential carbon mineralisation, however, a more systematic fluid composition analysis before and after CO_2 exposure is required to prove carbonate formation.

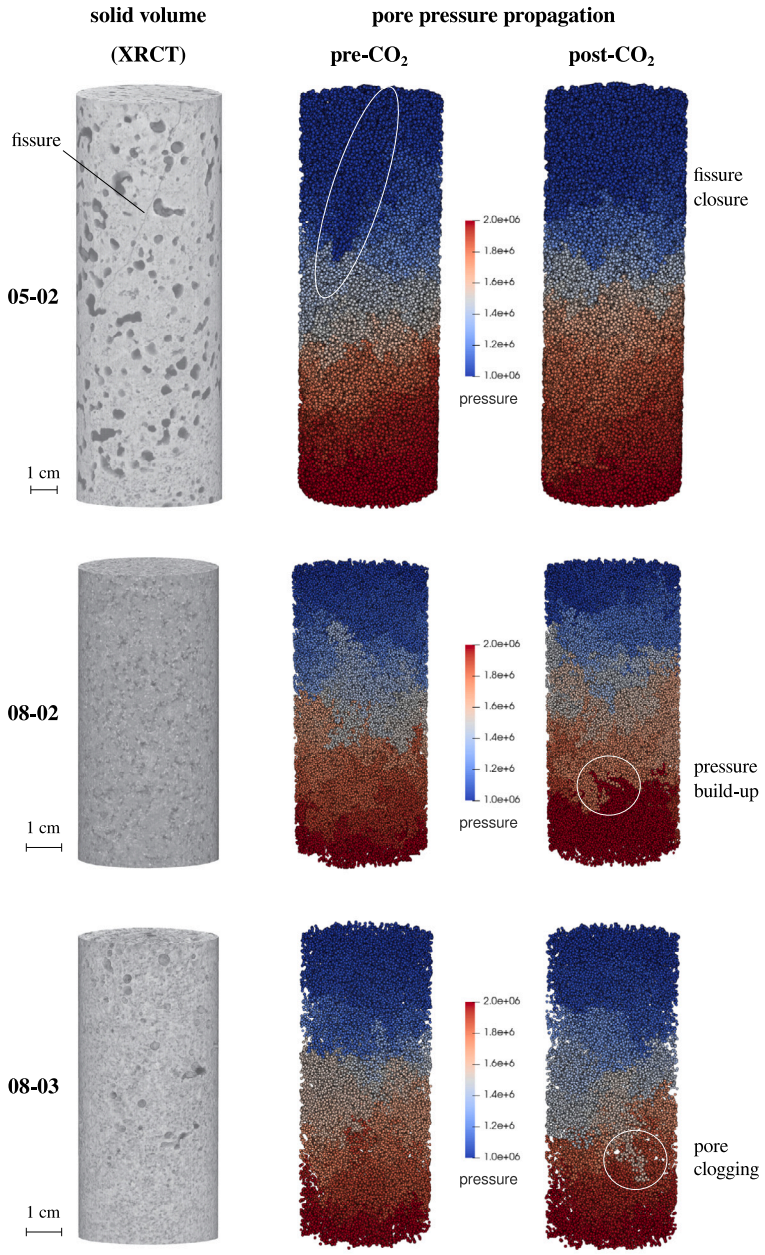

Fig. 8. Pore pressure propagation before and after CO_2 exposure. The existence of a micro-fissure in sample 05-02 is indicated.

Implications for CO_2 storage

The efficiency of CO_2 mineralisation in basalts relies on the availability of reactive minerals, subsurface conditions (e.g. pressure, temperature), carbonic fluid properties (e.g. CO_2 content, water composition) and reservoir characteristics (e.g. porosity, permeability) (Raza et al., 2022). Callow et al. (2018) underlined that pore clogging could be a major concern for CO_2 storage in basalts, pointing out that aspects related to clay swelling and re-mobilisation (in particular under high salinity conditions) are necessary for assessing the CO_2 potential of a reservoir.

Given the decrease in hydraulic conductivity (K), permeability (k) and electrolytic conductivity, as well as pH increase in our experimental study, carbon mineralisation seems to take place in intact basaltic cores already after two months of exposure to CO_2-rich seawater. The applied differential pressure (3.5 MPa) suits subsurface conditions, although the used CO_2 concentration is considerably higher than that in the Carbfix injection. Moreover, in-situ temperature (50 °C) is higher than that of our experiments (≈ 20 °C).

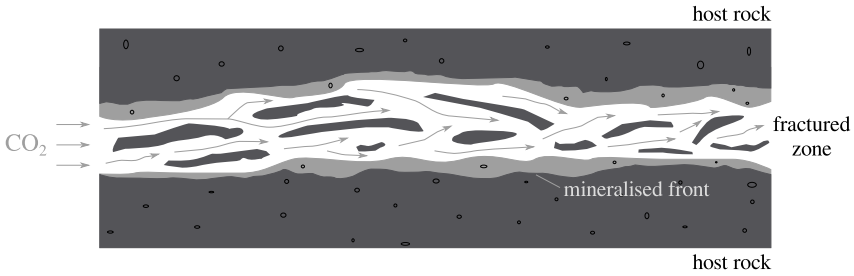

Fig. 9. Suggested illustration of carbon mineralisation front in the field.

Overall, the findings of this campaign show that in the intact zones of the basaltic reservoir, mineralisation can take place rapidly already after two months of CO_2 exposure. On the other hand, the obtained hydromechanical results show that carbon mineralisation leads to reduced flow properties that can lead to pore clogging and threaten storage efficiency. There is, therefore, high storage potential in the host rock on the condition that flow is not ceased, not only to ensure that the injected carbonic fluid will be able to reach unreacted rock zones, but also to avoid localised overpressure creation and potential triggering of micro-seismicity events. In our study, the basalt cores we tested are representative of intact rock in the field, regardless the pre-existing micro-fissure in sample 05-02. Given the relatively low levels of permeability we have measured, to ensure flow on site, injection in fractured zones is indispensable (Ratouis et al., 2022). Based on our results, mineralisation of the intact rock matrix would create a mineralised front driven by the connected micro-porosity. This front could further increase storage safety by prohibiting possible buoyancy movement of the carbonic fluid related to temperature differences between the injected fluid and the in-situ pore fluid (see suggested illustration in Fig. 9).

5. Conclusions

The acquired experimental and modelling results provide new insights into the occurrence of possible carbon mineralisation within basalt pore structure, considering macro- and micro-porosity. The key findings can be summarised as follows:

- Carbon mineralisation in the basaltic samples is inferred during two months of exposure to CO_2-rich seawater. Mineralisation was deduced from permeability reduction by half to one order of magnitude in three out of seven tested basaltic samples.
- Reduction of the flow properties between one and two months of exposure to dissolved CO_2 occurred in a pre-fissured and in the intact basaltic cores, respectively. Qualitative analysis of XRCT images of the fissured core before and after CO_2 exposure showed zones of decreased fissure aperture.
- 3D image analysis of X-ray tomographies of two intact samples (08-02 and 08-03) before and after CO_2 exposure showed reduction of up to 1.5% in macro-porosity for a pixel size of 50 μm.
- Pore network modelling to reproduce and analyse the experimental flow results included a double-scale porosity: macro-porosity (> 50 μm) and micro-porosity (< 50 μm). Two cases have been considered to account for the solid matrix micro-porosity, assigning a single pore size (d) and a lognormal pore size distribution ($\text{mean\_d} = \exp(\mu_d + \frac{\sigma_d^2}{2})$). The best fitted pore size diameters ($\text{d} \approx \text{mean\_d} \approx 2.5$ μm to 6.6 μm) are representative of the dominant pore size of the basalt measured with MIP.
- Macro-porosity reduction measured by XRCT did not have any significant impact on the simulated fluid flow. Reduction of the micro-porosity by up to 43% (corresponding to 2.2% decrease in total porosity) was required to reproduce the post-CO_2 experimental results. This suggests that carbon mineralisation is more prone to occur in the micro-pores of the basalt rather than in macro-pores (> 50 μm).
- Changes in the pore pressure distribution before and after CO_2 exposure revealed that structural modification took place in the material during CO_2 exposure. The localised zones of pressure build-up and discontinuous pressure propagation were not affected by the introduced variability of the assigned micro-porosity distribution. The observed evolution of the pore pressure front is another indication that mineralisation has occurred.

The overall findings of this work indicate that carbon mineralisation can occur when CO_2-rich seawater interacts with basalt. Mineralisation can have a significant impact on the flow properties of the intact basaltic material by reduction of micro-porosity. This suggests that large-scale implementation of the technology needs to be in a way that can tolerate significant permeability reduction, e.g. by injecting into highly permeable locations, ideally in fractured zones.

CRediT authorship contribution statement

Eleni Stavropoulou: Writing – review & editing, Writing – original draft, Visualization, Supervision, Methodology, Investigation, Formal analysis, Data curation, Conceptualization. **Cesare Griner:** Formal analysis. **Lyesse Laloui:** Supervision.

Declaration of competing interest

The authors declare that they have no known competing financial interests or personal relationships that could have appeared to influence the work reported in this paper.

Data availability

The 3D x-ray images used as inputs for the pore network simulations are provided online in Zenodo https://zenodo.org/doi/10.5281/zenodo.10910995. Additional data or results can be provided by the Authors upon reasonable request.

Acknowledgements

This study has taken place in the frame of the DemoUpStorage project that was funded by the Swiss Federal Office of Energy (SFOE). The Authors wish to thank Carbfix for providing the basalt cores, as well as the PIXE platform (EPFL) for the assistance during the X-ray tomography scans. Special thanks to Julien Andres from UniL for helping with the fluid analysis measurements. Last but not least, the Authors wish to deeply thank the Reviewers for their extensive and constructive feedback.

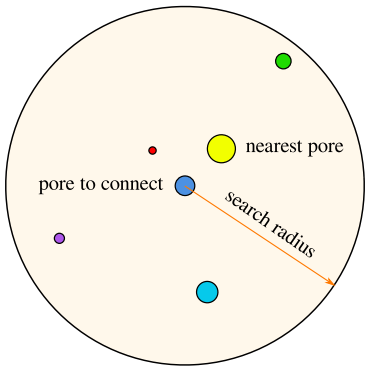

Fig. A.10. Illustration of manual pore connection method.

Table A.6
Number of pores and throats of the initial and fully connected networks.

		05-02		08-02		08-03	
		pre-CO_2	post-CO_2	pre-CO_2	post-CO_2	pre-CO_2	post-CO_2
initial network	pores	107619	147874	83837	77408	35564	30493
	throats	58500	90213	71770	80489	7471	6208
connected network	pores	107619	147871	82027	76844	35160	30111
	throats	260096	326166	217917	139941	140870	118498

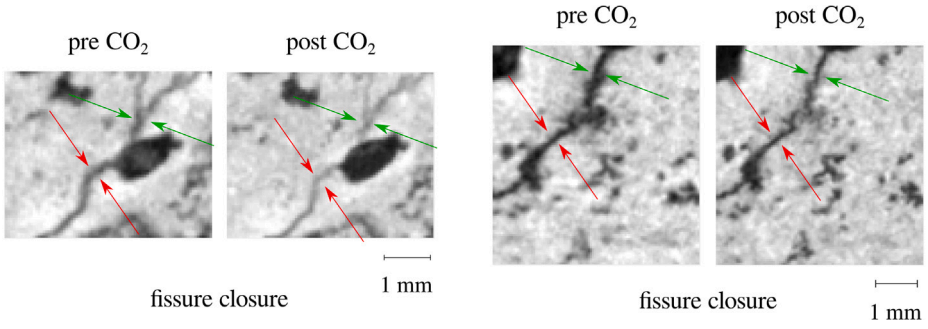

Fig. A.11. Magnified locations showing micro-fissure evolution of sample 05-02 before and after CO_2 exposure.

Appendix A. Pore connection methodology

To obtain a fully connected network, the non-connected pores of the network produced by the SNOW algorithm is manually connected. The used software distinguishes two types of non-connected pores: isolated and disconnected clusters of pores. The isolated pores are single pores that are not connected to any other pores. The disconnected clusters of pores are a group of pores that are not connected to other existing cluster in the network. Each type of not connected pore is connected to the closest pore in a different way.

Each isolated pore is connected to the nearest pore using an increasing search radius in 3D (see illustration in Fig. A.10). For the disconnected pore clusters, their connection to the nearest pore has an additional condition to avoid an over-connected network. Using an increasing search radius, the disconnected pore is connected to the nearest pore as long as it belongs to a different cluster of pores. Geometrical properties are then assigned to the added connections (throats) in order to perform the flow simulation.

The pore network properties (pore and throat number) of the initially generated network and the fully connected network the three samples before and after CO_2 exposure are presented in Table A.6. For the record, the minimum and maximum pore (sphere) diameters are 23 μm and 3938 μm for sample 05-02, 19 μm and 1671 μm for sample 08-02, and 17 μm and 3090 μm for sample 08-03. The minimum and maximum throat (cylinder) diameters are 18 μm and 1300 μm for sample 05-02, 9 μm and 380 μm for sample 08-02, and 8 μm and 812 μm for sample 08-03.

Appendix B. Micro-fissure evolution after CO_2 exposure

A number of micro-fissures were visible in sample 05-02 at the given scanning resolution. Given the mineralogical heterogeneity of the material, accurate segmentation of the fissures is not straightforward. Even though a 3D quantitative analysis is difficult to identify micro-fissure evolution, a qualitative fissure closure can be observed in zoomed areas of the sample. Two such zones are displayed in Fig. A.11, where a micro-fissure closure before and after CO_2 exposure is apparent. The nature behind this fissure evolution is unclear as it could be attributed either to the application of mechanical load during the lab testing, or as the result of carbon mineralisation on the fissure surface (higher specific surface area). Additional measurements at higher resolutions (e.g. SEM) could shed more light into the closure of fissures.

Appendix C. Pore pressure front

To evaluate the impact of a variable pore size distribution of the assigned micro-porosity on the localised pore pressure propagation, the post-CO_2 network is generated multiple times. Fig. 12 shows the pore

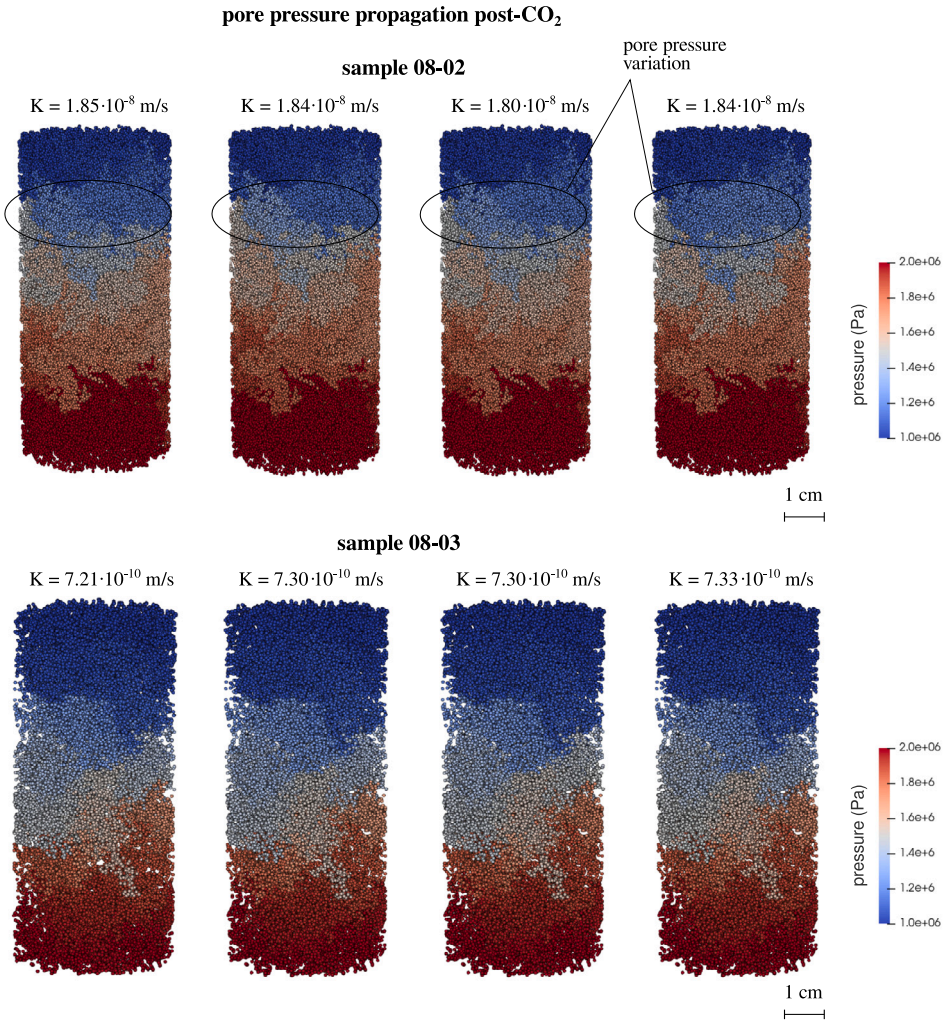

Fig. 12. Generated post-CO_2 pore pressure front and corresponding total hydraulic conductivity for samples 08-02 and 08-03.

pressure front of samples 08-02 and 08-03 generated four times and the corresponding values of the calculated hydraulic conductivity.

In both samples, the form of the propagation front is not affected by the variability of the pore size distribution. The variability introduced in the resulting network slightly manifests in the pore pressure level, mostly on the outflow side of sample 08-02 (top part). This is even less obvious for sample 08-03, where the pressure variation between the four generated networks is nearly undetectable. The reproducible localisation of pressure build-up and pore clogging (Fig. 8) is the result of the post-CO_2 exposure X-ray tomography of the sample.

References

Aradóttir, E.S., Sigurdardóttir, H., Sigfússon, B., Gunnlaugsson, E., 2011. CarbFix: a CCS pilot project imitating and accelerating natural CO2 sequestration. Greenh. Gases: Sci. Technol. 1 (2), 105–118.

Aradóttir, E.S.P., Sonnenthal, E.L., Björnsson, G., Jónsson, H., 2012. Multidimensional reactive transport modeling of CO2 mineral sequestration in basalts at the Hellisheidi geothermal field, Iceland. Int. J. Greenh. Gas Control 9, 24–40.

Becattini, V., Gabrielli, P., Antonini, C., Campos, J., Acquilino, A., Sansavini, G., Mazzotti, M., 2022. Carbon dioxide capture, transport and storage supply chains: optimal economic and environmental performance of infrastructure rollout. Int. J. Greenh. Gas Control 117, 103635.

Callow, B., Falcon-Suarez, I., Ahmed, S., Matter, J., 2018. Assessing the carbon sequestration potential of basalt using X-ray micro-CT and rock mechanics. Int. J. Greenh. Gas Control 70, 146–156.

Clark, D.E., Galeczka, I.M., Dideriksen, K., Voigt, M.J., Wolff-Boenisch, D., Gislason, S.R., 2019. Experimental observations of CO2-water-basaltic glass interaction in a large column reactor experiment at 50 C. Int. J. Greenh. Gas Control 89, 9–19.

Darcy, H.P.G., 1856. Les Fontaines publiques de la ville de Dijon. In: Exposition Et Application Des Principes À Suivre Et Des Formules À Employer Dans Les Questions De Distribution D'eau, Etc. V. Dalamont.

De Paolo, D.J., Thomas, D.M., Christensen, J.N., Zhang, S., Orr, F.M., Maher, K., Beson, S., Lautze, N., Xue, Z., Mito, S., 2021. Opportunities for large-scale CO2 disposal in coastal marine volcanic basins based on the geology of northeast Hawaii. Int. J. Greenh. Gas Control 110, 103396.

Farooqui, M.Y., Hou, Huijun, Li, Guoxin, Machin, Nigel, Neville, Tom, Pal, Aditi, Shrivastva, Chandramani, et al., 2009. Evaluating volcanic reservoirs. Oilfield Rev. 21 (1), 36–47.

Fisher, A.T., 1998. Permeability within basaltic oceanic crust. Rev. Geophys. 36 (2), 143–182.

Gislason, S.R., Broecker, W.S., Gunnlaugsson, E., Snæbjörnsdóttir, S., Mesfin, K.G., Alfredsson, H.A., et al., 2014. Rapid solubility and mineral storage of CO2 in basalt. Energy Procedia 63, 4561–4574.

Goldberg, D.S., Takahashi, T., Slagle, A.L., 2008. Carbon dioxide sequestration in deep-sea basalt. Proc. Natl. Acad. Sci. 105 (29), 9920–9925.

Gostick, J.T., 2017. Versatile and efficient pore network extraction method using marker-based watershed segmentation. Phys. Rev. E 96 (2), 023307.

Gostick, J., Aghighi, M., Hinebaugh, J., Tranter, T., Hoeh, M.A., Day, H., Spellacy, B., Sharqawy, M.H., Bazylak, A., Burns, A., Lehnert, W., 2016. OpenPNM: a pore network modeling package. Comput. Sci. Eng. 25 18 (4), 60–74.

Gysi, A.P., Stefánsson, A., 2012. CO2-water-basalt interaction, low temperature experiments and implications for CO2 sequestration into basalts. Geochim. Cosmochim. Acta 81, 129–152.

Khatiwada, M., Adam, L., Morrison, M., Wijk, K.van., 2012. A feasibility study of time-lapse seismic monitoring of CO2 sequestration in a layered basalt reservoir. J. Appl. Geophys. 82, 145–152.

Liu, D., Agarwal, R., Li, Y., Yang, S., 2019. Reactive transport modeling of mineral carbonation in unaltered and altered basalts during CO2 sequestration. Int. J. Greenh. Gas Control 85, 109–120.

Marieni, C., Henstock, T.J., Teagle, D.A., 2013. Geological storage of CO2 within the oceanic crust by gravitational trapping. Geophys. Res. Lett. 40 (23), 6219–6224.

Matter, J.M., Broecker, W.S., Stute, M., Gislason, S.R., Oelkers, E.H., Stefánsson, A., Wolff-Boenisch, D., Gunnlaugsson, E., Axelsson, G., Björnsson, G., 2009. Permanent carbon dioxide storage into basalt: the CarbFix pilot project. Iceland. Energy Procedia 1 (1), 3641–3646.

Matter, J.M., Stute, M., Snæbjörnsdottir, S.Ó., Oelkers, E.H., Gislason, S.R., Aradottir, E.S., et al., 2016. Rapid carbon mineralization for permanent disposal of anthropogenic carbon dioxide emissions. Science 352 (6291), 1312–1314.

McGrail, B.P., Schaef, H.T., Spane, F.A., Horner, J.A., Owen, A.T., Cliff, J.B., et al., 2017. Wallula basalt pilot demonstration project: post-injection results and conclusions. Energy Procedia 114, 5783–5790.

Ratouis, T.M., Snæbjörnsdóttir, S.Ó., Voigt, M.J., Sigfússon, B., Gunnarsson, G., Aradóttir, E.S., Hjörleifsdóttir, V., 2022. Carbfix 2: A transport model of long-term CO2 and H2S injection into basaltic rocks at Hellisheidi, SW-Iceland. Int. J. Greenh. Gas Control 114, 103586.

Raza, A., Glatz, G., Gholami, R., Mahmoud, M., Alafnan, S., 2022. Carbon mineralization and geological storage of CO2 in basalt: Mechanisms and technical challenges. Earth-Sci. Rev. 229, 104036.

Renard, P., Genty, A., Stauffer, F., 2001. Laboratory determination of the full permeability tensor. J. Geophys. Res.: Solid Earth 106 (B11), 26443–26452.

Saar, M.O., Manga, M., 1999. Permeability-porosity relationship in vesicular basalts. Geophys. Res. Lett. 26 (1), 111–114.

Sharqawy, M.H., Lienhard, J.H., Zubair, S.M., 2010. Thermophysical properties of seawater: a review of existing correlations and data. Desalination Water Treat. 16 (1–3), 354–380.

Sigfusson, B., Gislason, S.R., Matter, J.M., Stute, M., Gunnlaugsson, E., Gunnarsson, I., et al., 2015. Solving the carbon-dioxide buoyancy challenge: The design and field testing of a dissolved CO2 injection system. Int. J. Greenh. Gas Control 37, 213–219.

Snæbjörnsdóttir, S.Ó., Gislason, S.R., Galeczka, I.M., Oelkers, E.H., 2018. Reaction path modelling of in-situ mineralisation of CO2 at the CarbFix site at Hellisheidi, SW-Iceland. Geochim. Cosmochim. Acta 220, 348–366.

Snæbjörnsdóttir, S.Ó., Oelkers, E.H., Mesfin, K., Aradóttir, E.S., Dideriksen, K., Gunnarsson, I., et al., 2017. The chemistry and saturation states of subsurface fluids during the in situ mineralisation of CO2 and H2S at the CarbFix site in SW-Iceland. Int. J. Greenh. Gas Control 58, 87–102.

Snæbjörnsdóttir, S.Ó., Sigfússon, B., Marieni, C., Goldberg, D., Gislason, S.R., Oelkers, E.H., 2020. Carbon dioxide storage through mineral carbonation. Nat. Rev. Earth Environ. 1 (2), 90–102.

Voigt, M., Marieni, C., Baldermann, A., Galeczka, I.M., Wolff-Boenisch, D., Oelkers, E.H., Gislason, S.R., 2021. An experimental study of basalt-seawater-CO2 interaction at 130 °C. Geochim. Cosmochim. Acta 308, 21–41.

White, S.K., Spane, F.A., Schaef, H.T., Miller, Q.R., White, M.D., Horner, J.A., McGrail, B.P., 2020. Quantification of CO2 mineralization at the Wallula basalt pilot project. Environ. Sci. Technol. 54 (22), 14609–14616.

Wu, H., Jayne, R.S., Bodnar, R.J., Pollyea, R.M., 2021. Simulation of CO2 mineral trapping and permeability alteration in fractured basalt: Implications for geologic carbon sequestration in mafic reservoirs. Int. J. Greenh. Gas Control 109, 103383.

Zahasky, C., Thomas, D., Matter, J., Maher, K., Benson, S.M., 2018. Multimodal imaging and stochastic percolation simulation for improved quantification of effective porosity and surface area in vesicular basalt. Adv. Water Resour. 121, 235–244.

Zappone, A., Wiemer, S., et al., 2023. The DemoUpStorage Project: monitoring mineral carbonation in Icelandic basalts (No. EGU23-14256). In: Copernicus Meetings.